Nyiragongo crater collapses measured by multi-sensor SAR amplitude time series

D. Smittarello[1], R. Grandin[2], M. Jaspard[1], D. Derauw[3,4], N. D'Oreye[1,5], T. Shreve[6,7], M. Debret[8], N. Theys[9], H. Brenot[9]

[1]European Center for Geodynamics and Seismology, Walferdange, Grand Duchy of Luxembourg
[2]Université Paris Cité, Institut de Physique du Globe de Paris, CNRS, F-75005 Paris France
[3]Centre Spatial de Liège, Université de Liège, Angleur, Belgium
[4]Universidad Nacional de Río Negro. Instituto de Investigación en Paleobiología y Geología. de Río Negro-CONICET, General Roca, Argentina
[5]National Museum of Natural History, Department of Geophysics/Astrophysics, Walferdange, Grand Duchy of Luxembourg
[6]Earth and Planets Laboratory, Carnegie Institution for Science, Washington, DC. U.S.A.
[7]Geophysical Institute, University of Alaska Fairbanks, Fairbanks, Alaska, U.S.A.
[8]École et observatoire des sciences de la Terre. Université de Strasbourg. F-67084 Strasbourg, France
[9]Royal Belgian Institute for Space Aeronomy (BIRA-IASB), Brussels, Belgium

Key Points:

- Multi-sensor SAR amplitude images provide dense time series of Nyiragongo crater during the 2021 progressive collapse
- Nyiragongo crater was 270 m deeper after the 2021 eruption than after the 2002 eruption
- PickCraterSAR is a simple open-access interactive tool in Python to analyze images in multiples SAR geometries

Corresponding author: D. Smittarello, `delphine.smittarello@ecgs.lu`

Abstract

Crater morphology at active volcanoes can change rapidly. Quantifying changes during the course of a volcanic unrest episode may help assess the level of volcanic activity. However, limitations such as crater accessibility, cloud cover or intra-crater eruptive activity may hamper regular optical or on-site crater monitoring. Here we use multi-sensor satellite Synthetic Aperture Radar (SAR) imagery to produce dense time series of quantitative indicators of crater morphological changes. High temporal resolution is achieved by combining images from a variety of sensors and acquisition modes, though the diversity of acquisition geometries (incidence angle, viewing direction, resolution...) prevents direct comparison between the different images. Using basic trigonometry assumptions, we develop PickCraterSAR, an open-access tool written in Python to measure crater radius and depth from SAR amplitude images in radar geometry. We apply our methodology to study the crater collapse associated with the May 2021 and January 2002 eruptions of Nyiragongo volcano. After the 2021 collapse, we estimate the maximum depth of the crater to be 850 m below the rim and the total volume to be 84±10 Mm^3 (270 m deeper but only 15-20 % more voluminous than the post-2002 eruption crater). We also show that the 2021 crater collapse occurred progressively while a dike intrusion was migrating toward the south.

Plain Language Summary

Changes in crater morphology provide important hints to assess the activity of a volcano. In addition to optical and thermal imagery, radar images are useful to monitor the crater as they are not limited by daylight and cloud cover conditions. Unlike in optics, where pixels are located in the picture depending on their viewing angle, pixels are located on radar images depending on their distance to the satellite. In the presence of topography, this causes geometric distortions (shortening and layover), which complicates the interpretation of the images. PickCraterSAR, an interactive Python tool, was designed to assist the interpretation of those images and, based on simple trigonometry assumptions, to extract indicators of the crater radius and depth. Dense time series are obtained by mixing images acquired by various sensors in different viewing geometries. We apply this methodology to measure changes in Nyiragongo crater associated to the 2021 eruption. We show that the crater collapse is significantly deeper but only 15-20 % more voluminous than the 2002 collapse. Moreover, we can quantify the progression of the crater collapse that occurred after the 2021 eruption, while a magma intrusion was migrating underground southward for about a week.

1 Introduction

1.1 SAR amplitude imagery for volcano monitoring

Satellite imaging of the Earth has become a game changer over the last decades in many fields, including volcanology. Space-borne observation systems complement ground-based monitoring methods, especially when conditions are hazardous. Unlike other imagery, Synthetic Aperture Radar (SAR) provides day and night measurements, whatever the cloud cover. Probably the most popular applications of SAR imagery for volcano monitoring uses the monochromatic and coherent properties of the radar signal to produce interferograms (InSAR), which measure ground displacement (Massonnet & Feigl, 1998).

Over the last two decades, several new methods using SAR amplitude images were developed to monitor various features of volcanic activity. These studies include mapping of fresh lava (e.g., Wadge et al., 2012), explosive deposits (Dualeh, Ebmeier, Wright, Albino, et al., 2021), or more recently eruptive vent alignment (Muñoz et al., 2022). More-

over, because the radar signal travels along a straight path like in optics, it can be blocked by sub-vertical features, creating shadows. This characteristic has been exploited to extract quantitative features of interest from images– for example, Wadge et al. (2012) used SAR shadows to measure lava thickness. During unrest or eruption, key information can be provided by studying crater morphology. At explosive volcanoes, this mainly consists of dome growth measurements, to anticipate explosions and pyroclastic flows (e.g., Pallister et al., 2013). At some effusive volcanoes with lava lake activity, SAR shadows have been used to measure lava lake height within Nyiragongo crater (SAsha method) (Barrière et al., 2018, 2022) or at Erta Ale (Moore et al., 2019).

However, these shadow-based methods have important limitations. Unlike in optics where pixels are located in the image depending on their viewing angle, pixels in radar images are instead located depending on their distance to the satellite along a profile perpendicular to the satellite orbit. In the presence of topography, this causes severe geometric distortions, namely foreshortening (e.g. when the summit and the base of a relief are nearly at the same distance from the satellite) and layover (e.g. when the summit of the relief is closer to the satellite and appears before its base on the image). Also, when two or more points are located at the same distance from the satellite, they are indiscernible on the SAR image. Hence, when a crater is too narrow and/or too deep, or if the incidence angle is too steep, these distortions will hamper the detection and measurement of the shadows.

In addition, the ever-increasing frequency of SAR image acquisitions, thanks to the rapid development of new sensors and satellites, offers unprecedented opportunities to build high temporal resolution time series. However, these sensors often have different characteristics and viewing geometries. Combining sensors with different acquisition geometries is hence rarely trivial due to the various distortions (Dualeh, Ebmeier, Wright, Poland, et al., 2021).

The proposed method offers a solution to these limitations and the provided Python software assists image analysis, regardless of acquisition geometry.

1.2 Nyiragongo volcanological context

Nyiragongo is a strato-volcano (3500 m above sea level) standing in the Virunga Volcanic Province, in the western branch of the East African Rift Zone. It is located in a region at the border between the Democratic Republic of Congo, Uganda and Rwanda, affected by more than 20 years of armed conflicts and insecurity (Liégeois & Luntumbue, 2022). This, added to the natural intrinsic difficulties encountered in that region (equatorial vegetation, lightning, intense rain...), makes it a challenging region for volcano monitoring.

Over the past century, Nyiragongo hosted the largest long-lived lava lake on Earth (Lev et al., 2019) and its eruptive activity occurred mainly within the crater (Barrière et al., 2022). Prior to the 2021 eruption, only two historical flank eruptions were recorded– in 1977 (Tazieff, 1977) and 2002 (Komorowski et al., 2002; Wauthier et al., 2012). The third historical flank eruption that occurred on 22 May 2021 (Smittarello et al., 2022) was the first ever monitored at Nyiragongo using a ground network and space-borne instruments. Interestingly, these three flank eruptions were all associated with a crater collapse. In 1977, the crater floor, which had reached the elevation of ∼3270 m before the eruption, collapsed down to 2620 m (Pottier, 1978). In 2002, the crater floor that had been at ∼3190 m since 1995 collapsed to 2880 m (Barrière et al., 2022). In May 2021, the active lava lake started to overflow the remnant platform of the post-2002 crater floor. It was hence at the altitude of ∼3190 m when the 2021 eruption started and a new crater collapse occurred. The effusive episode of May 2021 eruption was short, with lava erupting from fissures for less than 6 hours. In contrast, intense seismic activity and ground deformation continued for about a week. Analysis of these measurements clearly revealed

a dike intrusion propagating southward from Nyiragongo beneath Goma city (Smittarello et al., 2022). Detailed analysis of the crater morphology showed that the collapse crater enlarged (in width and depth) during the course of the dike propagation phase. However, the precise temporal relationship between crater enlargement and dike propagation remains poorly resolved.

In the following section, we present the SAR images that we use to track and measure the crater collapse associated with the 2021 eruption, as well as the images used to confirm the 2002 collapse depth.

2 Data

The 2021 collapse was imaged by various SAR sensors onboard 7 different satellite constellations: ALOS–2, COSMO-SkyMed (CSK), Capella, ICEYE, Radarsat Constellation Mission (RCM), Sentinel–1 (S1) and TerraSAR–X (TSX), providing us with 44 images acquired between 2021-05-13 and 2021-07-06 along 17 different geometries (Tab. 1). In this study, we use this unique, dense time series of observations to quantitatively reconstruct the crater collapse.

Merging these data into a uniform time series is challenging, because it requires combining a broad variety of image characteristics. Images are acquired in X, C and L bands, either in Spotlight, Stripmap or TopSAR acquisition mode, thus with resolution ranging from 20 cm to 15 m. We also have to deal with various incidence angles ranging from 21.5° for the steepest to 53.5° for the flattest, and various viewing directions along both ascending and descending orbits, either right- or left-looking.

For the 2002 eruption, we use 18 images acquired by 3 satellites (ERS, RADARSAT-1 and ENVISAT), all acquired in C band, though with various incidence angles and orbital characteristics (Tab. 1).

The complete lists of all SAR images used in this study and their characteristics are available in Supplementary Tab. S1 and S2.

Table 1. List of SAR sensors and modes used to study the Nyiragongo crater collapse

Satellite	Total images	Modes	Band	First image	Last image
ERS	13	2	C	2000-09-28	2003-04-09
ENVISAT	1	1	C	2003-12-26	2003-12-26
RADARSAT-1	4	2	C	2001-03-22	2002-01-28
Total	**18**	**5**		**2000-09-28**	**2003-12-26**
ALOS–2	2	2	L	2021-05-28	2021-06-03
CSK	12	2	X	2021-05-16	2021-07-03
Capella	2	2	X	2021-05-23	2021-05-26
ICEYE	4	4	X	2021-05-25	2021-06-05
RCM	3	3	C	2021-05-24	2021-05-25
S1	16	2	C	2021-05-13	2021-07-06
TSX	5	2	X	2021-05-24	2021-06-22
Total	**44**	**17**		**2021-05-13**	**2021-07-06**

Figure 1. Set up. (a) Schematic of the simplified geometry of Nyiragongo topography. (b) Close up view of the collapsed crater. See parameter description in Tab. 2. (c) Nyiragongo crater seen from helicopter on the 5 November 2021. Credit J. Subira, Observatoire Volcanologique de Goma. P1 and P2 are the remnants of the platforms formed during the 1977 and 2002/2021 eruptions, respectively.

3 Methods

3.1 Theoretical framework

To facilitate the interpretation, we take advantage of the almost ideal shape of the upper part of Nyiragongo edifice, which makes it possible to describe the crater with a few parameters, whose values are given in Tab. 2. The topography of the edifice is modeled as a truncated cone whose radii are R_0 and $R_s < R_0$ and height is $Z_s - Z_0$ (Fig. 1a). Its cross section at the summit is almost circular. Before the 2021 collapse, the geometry of the inner crater was characterized by the presence of portions of annular platforms. These are fragments of the crater floor that remained attached to the walls after the 1977 and 2002 collapses. These platforms are labelled P1 and P2 respectively, while the bottom of the crater is labelled P3. From 2002 to 2021, the lava lake nested in P3 episodically overflowed and solidified on the surrounding crater floor, causing its progressive filling (Barrière et al., 2022). Shortly before the May 2021 eruption, P3 had reached the elevation of P2, at about 3190 m (Barrière et al., 2022). Neglecting the remnant batches of platform P1, the upper part of the main summit crater is modeled as a reversed truncated cone, whose radii are R_s and $R_{P2} < R_s$ and height is $Z_s - Z_{P2}$ (Fig. 1a). As shown in Fig. 1b, we also model the lower part of the crater, i.e. the collapsed crater, with a second truncated cone whose radii are R_c at the top and R_b at the bottom. Its depth H is referenced from P2. Note that if $R_b = R_c$, the crater would be a cylinder (Fig. S1a) and if $R_b = 0$ the crater would be a cone (Fig. S1c). Thus in the following, we consider $R_b = \alpha R_c$ with $\alpha \in [0 - 1]$.

Important assumptions in this geometrical simplification are that the main summit crater (blue circle in Fig. 2) and P2 platform (cyan circle in Fig. 2) are nearly horizontal, the top of the collapsed crater (red circle in Fig. 2) is also circular, nearly horizontal and located at the same elevation as the P2 platform at Z_{P2}, but its center (red star in Fig. 2) may be shifted horizontally with reference to the center of P2 by (δ_x, δ_y). The collapsed crater is supposed to be axi-symmetric– either a truncated cone or a cone (i.e. its bottom can be flat or a point). The bottom center (magenta star in Fig. 2) must coincide with the geographical position of the crater center at Z_{P2} (empty red star in Fig. 2). In the specific case of Nyiragongo, we assume that the main summit crater and P2 platform are centered, allowing measurements of the height between the summit and P2 using the same method as for measuring the depth of the collapsed crater.

3.2 Slant range projection

Because of radar imaging specificities, some trigonometry is required to translate observations made in slant range (i.e. radar geometry) into ground range geometry (i.e. projected on a ground plane).

3.2.1 Crater radius

To measure the collapsed crater radius, we assume that the edges of the main summit crater and collapsed crater are nearly horizontal and nearly circular. Thanks to this circular geometry in map view, their shape in radar geometry is expected to be ellipti-

Table 2. List of the geometrical parameters used for the modeling of Nyiragongo topography.

Symbol	Value	Unit	Description
R_0	2500	m	Radius at the base of the edifice
Z_0	2500	m	Elevation at the base of the edifice
R_s	675	m	Radius of the main summit crater
Z_s	3460	m	Elevation of the summit
R_{P2}	420	m	Radius of the platform P2
Z_{P2}	3190	m	Elevation of the platform P2
R_c	100 - 350	m	Radius of the collapse crater
R_b	0 - R_c	m	Radius of the collapse crater bottom
Z_b	$< Z_{P2}$	m	Elevation of the collapsed crater bottom
H	0-700	m	Collapsed crater depth with reference to platform P2 elevation
δ_x	0 - 100	m	Along range offset between main summit crater and collapse crater centers
δ_y	0 - 100	m	Along azimuth offset between main summit crater and collapse crater centers
α	0 - 1	n.d.	R_b/R_c

Figure 2. Methodology for estimating the collapsed crater radius and depth, assuming an idealized circular shape of the summit rim (blue), P2 platform (cyan), crater edge (red) and crater bottom (magenta). (a) Perspective view. (b) Map view. (c) Radar geometry view. (d) Cross section view. The incidence angle θ is counted negative for ascending right- or descending left-looking acquisition geometries and positive otherwise, 0 meaning vertical incidence. Stars and dots represent the centers and edges of the circular structures, respectively. Empty markers and filled markers represent the objects in 3D perspective view and in their slant range projection respectively.

cal, with the semi-axes of the ellipse oriented along the azimuth and range coordinates of the image (Fig. 2). The elliptical shape of the caldera in radar geometry provides a consistent reference for estimating the progressive broadening of the collapsing crater. In what follows, we note R the radius of the circular shape in map view (expressed in meters), and a and b the semi-axes lengths of the ellipse in radar geometry (expressed in number of pixels), respectively along the azimuth and range dimensions. The subscripts "s", "$P2$", "c" and "b" are used when referring to the edge of the summit crater rim, the outline of the P2 platform, the edge of the collapsed crater rim and the crater bottom respectively. The subscript "i" represents any of those.

The size of a pixel in the azimuth direction (i.e. in the heading direction of the satellite, ΔAz) remains the same in satellite and ground range geometry. However, the size of a pixel in the ground-range geometry, $\Delta GrRa$, is related to its size in slant-range $\Delta SlRa$ and the incidence angle θ (Eq. 1) as shown in the inset of Fig. 2:

$$\Delta GrRa = \frac{\Delta SlRa}{\sin\theta} \tag{1}$$

Hence, the size and shape of a circular feature seen in side view and expressed in slant range can be assessed as follows. The projection of the circular shape on the oblique-looking geometry effectively corresponds to an axis re-scaling proportional to the pixel size in slant-range $\Delta SlRa$ and incidence angle θ (Eq. 3) and on the pixel size in azimuth ΔAz (Eq. 2):

$$a_i = \frac{R_i}{\Delta Az}, \tag{2}$$

$$b_i = \frac{R_i}{\Delta GrRa} = \frac{R_i}{\left(\frac{\Delta SlRa}{\sin\theta}\right)}. \tag{3}$$

Depending on the ratio between $\frac{\Delta SlRa}{\sin\theta}$ and ΔAz, the ellipses may appear flattened in range (if $\frac{\Delta SlRa}{\sin\theta} > \Delta Az$) or in azimuth (if $\frac{\Delta SlRa}{\sin\theta} < \Delta Az$). As a consequence, the aspect ratio of all ellipses (main summit crater rim, P2 outline, collapse crater rim and crater bottom) only depends on the ratio between the pixel sizes, while the radius of the circle vanishes from the equation:

$$\frac{a_i}{b_i} = \frac{\Delta GrRa}{\Delta Az} = \frac{\Delta SlRa}{\Delta Az \sin\theta} \tag{4}$$

Unfortunately, the non-vertical incidence angle of the SAR images often produces geometric distortions in range (foreshortening, layover, shadowing), which makes it difficult to precisely pick the edge of the ellipses in the range direction for certain combinations of crater geometry versus acquisition geometry. In particular, images acquired with a steep incidence angle (close to vertical) will be affected by severe layover, distorting the shape of the crater and leading to substantial uncertainty in the contouring of the ellipses, especially in the range direction. Fortunately, no such a distortion affects the azimuth direction. As a result, the dimension of circular features such as the main summit crater can be identified with better confidence along the azimuth direction, which in turns allows us to make a reliable estimation of a_i. Knowing the aspect ratio of the ellipses, the value of b_i can be determined using Eq. 4, while Eq. 2 provides the real radius R_i.

3.2.2 Crater Depth

The depth of the crater can be estimated using two different methods: either by measuring in slant range the distance between the geometric center of the crater bottom and the center of the crater rim, or by measuring the distance between the close-range and far-range crater edges and the center of the crater bottom.

3.2.2.1 Method 1 slant range distance from crater center

The slant-range separation c between the geometric center of the crater bottom (magenta star in Fig. 2) and the geometric center of the crater rim (red star in Fig. 2) can be used to deduce the elevation difference H, by taking into account the incidence angle θ (Fig. 2):

$$H = \frac{c}{\cos\theta} \tag{5}$$

This equation holds under the condition that the two points lie at the same geographic coordinate, but at different altitudes, which can be satisfied as long as the crater has an axi-symmetric shape. On one hand, the center of the crater rim can be estimated by fitting an ellipse to its shape (Section 3.2.1). On the other hand, location of the crater bottom has to be picked. Assuming that the crater is conic, the layover would appear triangular and the crater bottom corresponds to the layover tip. However, if the crater shape is more like a truncated cone with a flat bottom which radius is R_b, the crater bottom can be found by fitting an ellipse of semi radii a_b and b_b and determining its center (Fig. 2),

$$b_b = R_b \sin\theta. \tag{6}$$

If one assume that the crater is conic while its real geometry is truncated with flat bottom, the systematic error made on H by picking the layover extremity instead of the layover ellipse center is δh :

$$\delta h = \frac{b_b}{\cos\theta} = R_b \tan\theta \tag{7}$$

223 *3.2.2.2 Method 2 slant range distances from crater edges*

Alternatively, instead of using the geometric center of the crater rim as a reference, one can use the slant range distances between the crater edges and the crater bottom center (distances e_1 and e_2 in Fig. 2) as a way to derive the crater depth H and crater internal slope angle φ. We can write:

$$\left.\begin{aligned} e_1 &= d_1 \cos(\varphi_1 - \theta) \\ H &= d_1 \cos\varphi_1 \end{aligned}\right\} \Longrightarrow H = e_1 \frac{\cos\varphi_1}{\cos(\varphi_1 - \theta)} \tag{8}$$

$$\left.\begin{aligned} e_2 &= d_2 \cos(\varphi_2 - \theta) \\ H &= d_2 \cos\varphi_2 \end{aligned}\right\} \Longrightarrow H = e_2 \frac{\cos\varphi_2}{\cos(\varphi_2 - \theta)} \tag{9}$$

Note that crater symmetry imposes $d_1 = d_2$ and $\varphi_1 = -\varphi_2$ and we can call them d and φ. Combining Eq. 8 and Eq. 9, we get:

$$\frac{e_1}{e_2} = \frac{\cos(\varphi - \theta)}{\cos(\varphi + \theta)} \tag{10}$$

Eq. 10 can be rewritten and factorized as:

$$(e_1 - e_2)\cos\varphi\cos\theta = (e_1 + e_2)\sin\varphi\sin\theta \tag{11}$$

Eq. 11 simplifies as:

$$\tan\varphi = \frac{1}{\tan\theta}\frac{e_1 - e_2}{e_1 + e_2} \tag{12}$$

224 Eq. 12 gives φ, the mean crater slope, which can be substituted into either Eq. 8 or Eq. 9
225 to determine H.

226 We note that the analysis holds whatever the internal shape of the crater, as long
227 as it remains axi-symmetric. For instance, if the internal crater shape is paraboloidal as
228 observed in reality at Nyiragongo (that is the crater slope is steeper than φ close to the
229 rim and flatter towards the bottom), the methods remains valid.

230 **3.3 Picking and amplitude simulation tools**

231 The above described methods are based on accurate measures performed in SAR
232 amplitude images in slant range geometry, which requires determining reliable position
233 of crater edges and centers. However, this task can be complicated by geometrical dis-
234 tortions, speckle noise in SAR amplitude signal or contrast changes between the crater
235 features depending on the viewing geometry. To assist these measurements, we devel-
236 oped PickCraterSAR (Fig. 3) and used it to analyze 62 SAR images of Nyiragongo crater.
237 PickCraterSAR is an open-source, interactive picking tool software written in Python
238 using the graphical interface library Qt through the module PyQt. It contains a main
239 module for picking positions and drawing ellipses on the SAR images (Fig. 3a). A sec-
240 ondary module assists the user by simulating slant range SAR amplitude images of the
241 simplified volcano as seen by the satellite (Fig. 3c), as well as a 3D model and a cross
242 section of the volcano locating the features chosen on the amplitude image (Fig. 3b and
243 d). The tool was developed for studying Nyiragongo volcano, and can be easily adapted
244 for others volcanoes hosting circular and axi-symmetric crater(s) by modifying the sim-
245 plified topography.

246 ***3.3.1 Picking tool***

247 PickCraterSAR loads an input text file containing the list of all SAR images in the
248 time series with their acquisition time and viewing characteristics (incidence angle, az-
249 imuth and slant range pixel sizes). The main module of PickCraterSAR consecutively
250 (Fig. 3a) displays one SAR image of the list for the user to manually pick 4 ellipses cor-
251 responding to the volcano circular features (respectively, the summit crater rim, P2 con-
252 tour, collapse crater rim and bottom). Coordinates of the picked ellipses are saved and

Figure 3. Screenshot of the PickCraterSAR Application. PickCraterSAR contains 5 displays. Main display shows the amplitude image and the picking tool (a). Others displays show the 3D-view of the crater model (b) and the along range cross-section view (d). An optional display represents the simulated amplitude corresponding to the 3D model(c). Last display shows the radii and elevation time series results (e).

Figure 4. Simplified amplitude simulation methodology. Topographic profile is regularly subsampled and each point is projected on the slant range direction. For each interval in slant range, we sum all individual contributions to get the simplified simulated amplitude.

Figure 5. Using ascending and descending LOS to determine crater asymmetry along range direction

added to the input file. A 3D model of the volcano (Fig. 3b) taking into account the picked elliptical features is computed according to the theoretical framework presented in Sections 3.1 and 3.2. Additionally, PickCraterSAR displays an elevation profile of the estimated crater in the along range direction (Fig. 3d). The last panel displays the radius and elevation times series (Fig. 3e). Note that we chose to pick only the diameter $2a_i$ of each ellipse in the azimuth direction as it is the least affected by distortions. From these two points, the software computes the position of the ellipse center and the radius R_i of the corresponding circle in perspective view according to Eq. 2. We take advantage of the quasi-circular shape of Nyiragongo to force the aspect ratio of the ellipses according to Eq. 4 and determine the ellipse range diameter $2b_i$. We compute crater depth H using Eq. 5 and uncertainties on H with Eq. 7. Note that instead of picking independently the crater center and edges, we derive the position of the center from picking the azimuth diameter, thus achieving the same results using Eq. 8 or Eq. 9 instead of Eq. 5. Using the appropriate picking strategy, one could use any of those equations.

3.3.2 Quick amplitude simulation tool

PickCraterSAR uses the methodology presented by (Dualeh, Ebmeier, Wright, Poland, et al., 2021) to compute the simplified simulated amplitude to assist the picking. It simulates the geometric contribution of the 3D model of the volcano crater to the amplitude image for each profile in the range direction. As shown in Fig. 4, for each profile it computes a series of simulated amplitude pixels as follows. First, it samples the modeled topographic profile at regular intervals (see dots in Fig. 4). Then it adds the individual contributions of each element along the topographic profile to each pixel in slant range. By aligning all these profiles along the azimuth direction, PickCraterSAR recreates the amplitude image simulating the contrasts observed in the SAR amplitude image (Fig. 3c).

3.4 The crater axi-symmetry hypothesis

The method assumes an axi-symmetric crater shape: the center of the crater at the level of its rim (Z_{P2}) and the center of the crater at its bottom must be vertically aligned. This is an important hypothesis. A shift in the position of the crater bottom center with respect to the crater center at Z_{P2} would be translated as a positive or negative error in the crater depth estimation depending on the looking direction (Fig. 5).

The following equations show that it is mandatory to have two viewing geometries to assess the impact of asymmetry on the depth estimation. Naming the mean slope of the crater as φ_1 on one side (edge with subscripts "1") and φ_2 on the other side (edge with subscripts "2"), we can estimate the slant range distances between both crater edges and the crater bottom center e_1 and e_2 and deduce the corresponding height estimates in a similar way as in Section 3.2.2.2 (Fig. 5). Subscripts "a" and "d" refer to the two viewing geometries (e_{1a} e_{2a}, e_{1d} and e_{2d}), which can be ascending and descending if the satellite is always looking to the same side, or two images acquired from the same side as long as their look angles are significantly different.

$$\left.\begin{aligned} e_{1a} &= d_1.\cos(\varphi_1 - \theta_a) \\ H_\varphi &= d_1.\cos(\varphi_1) \end{aligned}\right\} \Longrightarrow H_{\varphi_1} = e_{1a}.\frac{\cos(\varphi_1)}{\cos(\varphi_1 - \theta_a)} \tag{13}$$

$$\left.\begin{aligned} e_{2a} &= d_2.\cos(\varphi_2 - \theta_a) \\ H_\psi &= d_2.\cos(\varphi_2) \end{aligned}\right\} \Longrightarrow H_{\varphi_2} = e_{2a}.\frac{\cos(\varphi_2)}{\cos(\varphi_2 - \theta_a)} \tag{14}$$

$$\left.\begin{aligned} e_{1d} &= d_1.\cos(\varphi_1 - \theta_d) \\ H_\varphi &= d_1.\cos(\varphi_1) \end{aligned}\right\} \Longrightarrow H_{\varphi_1} = e_{1d}.\frac{\cos(\varphi_1)}{\cos(\varphi_1 - \theta_d)} \tag{15}$$

$$\left.\begin{aligned} e_{2d} &= d_2.\cos(\varphi_2 - \theta_d) \\ H_{\varphi_2} &= d_2.\cos(\varphi_2) \end{aligned}\right\} \Longrightarrow H_{\varphi_2} = e_{2d}.\frac{\cos(\varphi_2)}{\cos(\varphi_2 - \theta_d)} \tag{16}$$

where θ_a and θ_d are both incidence angles, d_1 and d_2 are the distance from the crater edge to crater bottom center and φ_1 and φ_2 are the average slope angle as defined in Fig. 5.

From Eq. 13 and Eq. 15, we get:

$$e_{1a}\cos(\varphi_1 - \theta_d) = e_{1d}\cos(\varphi_1 - \theta_a) \tag{17}$$

which can be expressed as:

$$e_{1a}(\cos\varphi_1\cos\theta_d + \sin\varphi_1\sin\theta_d) = e_{1d}(\cos\varphi_1\cos\theta_a + \sin\varphi_1\sin\theta_a) \tag{18}$$

Similarly, from Eq. 14 and Eq. 16, we get:

$$e_{2a}\cos(\varphi_2 - \theta_d) = e_{2d}\cos(\varphi_2 - \theta_a) \tag{19}$$

thus:

$$e_{2a}(\cos\varphi_2\cos\theta_d + \sin\varphi_2\sin\theta_d) = e_{2d}(\cos\varphi_2\cos\theta_a + \sin\varphi_2\sin\theta_a) \tag{20}$$

Combining Eq. 18 and Eq. 20, we get:

$$\begin{cases} \cos\varphi_1(e_{1a}\cos\theta_d - e_{1d}\cos\theta_a) = \sin\varphi_1(e_{1d}\sin\theta_a - e_{1a}\sin\theta_d) & (21) \\ \cos\varphi_2(e_{2a}\cos\theta_d - e_{2d}\cos\theta_a) = \sin\varphi_2(e_{2d}\sin\theta_a - e_{2a}\sin\theta_d) & (22) \end{cases}$$

So,

$$\begin{cases} \tan\varphi_1 = \dfrac{(e_{1a}\cos\theta_d - e_{1d}\cos\theta_a)}{(e_{1d}\sin\theta_a - e_{1a}\sin\theta_d)} & (23) \\ \tan\varphi_2 = \dfrac{(e_{2a}\cos\theta_d - e_{2d}\cos\theta_a)}{(e_{2d}\sin\theta_a - e_{2a}\sin\theta_d)} & (24) \end{cases}$$

Eq. 23 and Eq. 24 can be injected into Eq. 13 to Eq. 16 to provide estimates for H_{φ_1} and H_{φ_2}.

Provided that observations are performed from both viewing geometries, one can estimate the mean depth in an unbiased fashion using $H_{mean} = \frac{H_{\varphi_1} + H_{\varphi_2}}{2}$.

We can also quantify the crater asymmetry by computing ε as:

$$\varepsilon = \pm\frac{\varphi_1 + \varphi_2}{2} \tag{25}$$

such that $|\varepsilon|$ small means that the crater is symmetric and $|\varepsilon|$ increases when the crater becomes more asymmetric.

Figure 6. Time series of crater measures. Summit (dark blue), P2 (cyan), collapse crater (red) and bottom crater (magenta) radii (a) and elevation (b) time series obtained by manually picking 4 ellipses on each SAR image. Error bars in (a) represents 2, 3, 4 and 5 times the azimuth pixel size, respectively. Ash index computed using SEVIRI data spanning 13-05-2021 to 08-07-2021 from (Smittarello et al., 2022) is shown in gray. Error bars in (b) on Z_{P2} represents 5 times the range pixel size. Error bars on Z_b are computed using Eq. 7. In panel (b), green square mark values measured from both incidence angle, taking into account possible asymmetry of the crater. (c) Volume estimates derived from radius and elevation values for a truncated cone (black line). Square and dots are for measurements from negative and positive incidence angles, respectively. Minimum and maximum volume estimates corresponding to a cone (top gray triangles) and a cylinder (bottom gray cylinder), respectively, are also shown.

4 Results

4.1 Amplitude simulations

Simulating amplitude images helps to understand how geometric structures in Nyiragongo crater may contribute to the amplitude image distortions in slant range geometry, depending on the look angle. We simulated the amplitude image for each satellite geometry from our data set. We can observe that for the specific topography at Nyiragongo, the concentric elliptic structures (summit rim, P2 and crater edge) are less affected by distortions such as foreshortening and layover when the incidence angle is flat ($> 40°$). It is hence easy to pick the ellipse in these images. Conversely, we observe that the crater bottom is often confounded with P2 or the crater edge (Fig. S2d,e). Steeper incidence angles ($< 30°$) allow to better discriminate the location of the crater bottom, whatever the real crater shape is. However, those images are more affected by range distortions and the collapse crater edge can be almost totally hidden in the P2 layover (Fig. S2b), jeopardizing our ability to obtain an accurate picking. When distortions are strong and some structures are mixed together, in particular when the crater bottom cannot be clearly identified, the amplitude simulations provide a range of possible locations.

4.2 The progressive crater collapse associated with the May 2021 eruption

We analyzed 44 SAR images acquired before and after the May 2021 eruption of Nyiragongo. Picking the summit crater rim and P2 platform, which are mostly unaffected by the collapse, provided reference structures in all images. We measure the average summit crater and P2 radius to be $R_s = 675 \pm 5$ m and $R_{P2} = 450 \pm 15$ m respectively (Fig. 6). The average P2 elevation is $Z_{P2} = 3192 \pm 6$ m. The uncertainties correspond to the standard deviation computed for the corresponding measure using all the images. Moreover, the lava lake is clearly identifiable just before the 2021 eruption. Its radius was $\sim$100 m. The lava lake was drained during the eruption and left an empty and unstable pit. After its drainage, the crater radius R_c was 160 to 180 m on 23 May, then it further increased to 240 m during a collapse on the night from 23 May to 24 May. It remained stable up to 16:30 on 25 May when another significant collapse enlarged it to reach $\sim$ 350 m. Unstable crater walls continued to collapse during the following days and weeks but the mean radius did not significantly increase (Fig. 6). The depth of the crater was also measured with respect to P2. The lava lake drainage emptied the crater down to $Z_b \sim 2830$ m in the morning of 23 May. Then, as a result of collapse of unstable walls, its bottom was partially filled with rubble, making its depth rise up to $Z_b =$ 2930 m in the evening of 23 May. Progressive deepening resumed on 24 and 25 May when

the crater bottom was measured at an altitude of $Z_b \sim 2670 \pm 30$ m at 16:30 both with S1 and RCM images. On the same day, the ICEYE image acquired at 19:50 showed the crater refilled by ~ 200 m of rock debris resulting from the enlarging crater. Then the crater continued to deepen progressively, reaching its deepest point at $Z_b = 2610$ m on 30 May. After this date, the crater progressively refilled from collapsing walls and the bottom reached the altitude of 2780 m at the beginning of July (Fig. 6).

4.3 Validation with the 2002 crater collapse

In order to validate the proposed method with independent measures, we apply it to the crater depth at Nyiragongo after the January 17, 2002 eruption. The crater collapsed 5 days later, on January 22 (Durieux, 2002). Fortunately, a set of optical images were acquired by the IKONOS satellite on January 31, only 9 days after the collapse. Based on these images, processed with photogrammetric methods (Barrière et al., 2022), the crater bottom elevation was measured at 2880 ± 22 m. The same authors also process a layover-free ENVISAT image acquired on December 26, 2003 using the SASha method based on the length of the SAR shadow cast by the sub-vertical rim and obtained a similar value, that is 2872 ± 12 m (Barrière et al., 2022).

We processed 18 archive images from older SAR missions (ERS, RADARSAT-1, ENVISAT) with PickCraterSAR. On each of these images, we clearly identify the main summit crater and P2 platform and measure their radius as respectively $R_s = 676 \pm 7$ m and $R_{P2} = 484 \pm 11$ m. The crater collapse edge is also clearly visible and its radius is $R_c = 385 \pm 16$ m.

Finally, the measure of $R_b = 94 \pm 19$ m, $Z_{P2} = 3190 \pm 5$ and $H = 288 \pm 20$ m allow to deduce a mean crater bottom altitude of $Z_b = 2902 \pm 25$ m, which is in excellent agreement with the former estimates reported by (Barrière et al., 2022). Individual results for each images are shown in Supplementary Fig. S3.

5 Discussion

5.1 On the crater symmetry

We notice in Fig. 6 a systematic shift between depth estimates. Measurements from images with positive incidence angles (magenta empty top triangles) slightly overestimate the depth while images with negative incidence angles (magenta filled bottom triangles) underestimate the crater depth. Such a behavior could be explained by an asymmetric crater shape if the crater bottom center and crater edge center do not share the exact same geographical location (see section 3.4). Fortunately, five pairs of images were acquired from 2 sensors at very similar times but from different incidence angles:

1. TSX(AR -26°) and RCM (AR -41.5°) on 24 May (8 minutes)
2. S1(AR -34.02°) and RCM (AR -53.5°) on 25 May (8 minutes)
3. ALOS-2 (DR 41°) and ICEYE (DL -27°) on 28 May (116 minutes)
4. S1 (DR 39.36°) and CSK (AR -34.95°) on 08 June (18 minutes)
5. CSK(DR 26.06°) and TSX (AR -26°) on 15 June (36 minutes)

For each of those pairs, it is reasonable to assume that the crater shape did not evolve significantly between the image acquisitions.

Thus, we test the validity of the axi-symmetry hypothesis using these five pairs of images acquired at similar times. Results are shown in Supplementary Tab. S3 and with green squares on Fig. 6b. For all these dates when 2 images are available at the same time, we compute the depth taking into account the asymmetry (see green dots in Fig. 6). We note that the mean results are all within the error bars of the values previously ob-

tained. Thus, it validates our hypothesis and we can affirm that the new crater created by the collapse was almost symmetric when it formed. Nevertheless, we note that for the most recent pairs of images, there is a slight tendency toward an increase of the asymmetry. This could be due to a higher instability of a portion of the crater wall that would form scree preferentially in one direction. This hypothesis is confirmed by photos taken by helicopter in November 2021 (Fig. 1c).

5.2 On the crater collapse volume

As shown on Fig. 1a, we consider a collapse crater of total depth H modeled as a truncated cone which radii are R_c at the top and R_b at the bottom. The volume V_{trunc} of the crater can be expressed as :

$$V_{trunc} = \frac{\pi H R c^2}{3}\left(1 + \frac{R_b}{R_c} + \frac{R_b^2}{R_c^2}\right) \tag{26}$$

Writing $R_b = \alpha R_c$ with $\alpha \in [0, 1]$, Eq. 27 becomes:

$$V^{\alpha}_{trunc} = \frac{\pi H R_c^2}{3}\left(1 + \alpha + \alpha^2\right) \tag{27}$$

As shown on Fig. 6c, the crater stabilized after 28 May. The total volume can be computed accurately by averaging individual measurements made after this date, which gives an estimate of 84±10 Mm^3. Smittarello et al. (2022) modeled a 240 Mm^3 dike intrusion from Nyiragongo to the Lake Kivu. If we consider the volume lost in the crater as a minimum for the source deflation that fed the dike, we obtain a ratio $r_v \sim 2.9$ between the dike and the source lost volume. This apparent contradiction may indicate, at first sight, the existence of an additional source. However, a more careful analysis of deformation induced by dike intrusions suggests that the ratio $r_v \sim 2.9$ could be explained by the compressibility of a gas-poor magma (a feature of the Nyiragongo lava), without needing for an additional source of magma (Rivalta & Segall, 2008). For comparison, Barrière et al. (2018) estimate the volume of the lava lake to be 8 Mm^3 and the intra-crater cumulated volume to be ∼65-70 Mm^3 since 2002. Thus, at first order, the 2021 collapse volume has the same order of magnitude than the 2002 collapse. Even if it is ∼270 m deeper, due to the narrow conic shape at the bottom the volume increase represents only 15-20 %. Supplementary Fig. S4 shows an ERS image acquired after the 2002 collapse and a CSK image acquired in 2021 with a similar incidence angle revealing the striking differences between both collapse craters.

5.3 On the crater collapse mechanism

Fig. 6a also displays an ash index computed with SEVIRI data (Clarisse et al., 2013). According to this data, 3 peaks in ash emissions are clearly visible. The first one started around 07:30 on 23 May and the second around 06:15 on 25 May. The third significant peak around 04:30 on 29 May was smaller than the previous two. Ash emission peaks clearly precede by a few hours a significant increase in the crater radius and a decrease in the crater depth that could be related to large parts of P2 collapsing into the crater. Interestingly, during both events, SAR images were acquired after the ash peak, but before the collapse, clearly evidencing that the observed kilometer-high ash columns preceded the collapse. In other words, an internal explosion ejected material from the crater, producing the ash emissions. This void subsequently weakened the crater walls, leading to their collapse within a few hours after the explosions, without producing such significant ash emissions.

5.4 On the acquisition characteristics

In the framework of the Nyiragongo eruption, due to the activation of the International Charter Space and Major Disaters, a large number of SAR acquisition were made by a variety of satellites. Some of these acquisitions are part of the long-term regular monitoring of this volcano (mainly S1 and CSK images) but others are more occasional (ALOS-2, TSX). Some images were unique in their viewing geometry as they were acquired by very agile commercial satellites that responded to the emergency situation (e.g. Capella, ICEYE). This dataset is exceptional with respect to standards of previous decades, but may represent a glimpse into future acquisition capabilities of the global satellite constellation. Hence, experience gained from the study of the 2021 Nyiragongo eruption can be useful to draw lessons for future acquisition strategies in the context of volcanic unrest monitoring.

From our picking experience, we note that the high agility helps in providing dense time sampling. However, we also note that series of several images acquired in the same viewing geometry may be easier to interpret. When some features are hard to identify, such as the limit of a platform in a layover region, comparing successive images acquired in the same viewing geometry allows identifying minute variations of the amplitude associated with an evolving structure.

We also notice that low (steep) angles better separate the crater bottom from the inner crater structures while high (grazing) angles provide better view of the crater footprint. Moreover, images with a steeper incidence angle are less sensitive to the actual shape of the crater bottom, and are therefore likely to provide more robust estimates of the crater depth as long as the crater rim can still be identified accurately.

Regardless, being able to analyze jointly images with a variety of look angles diminishes the risk of including systematic errors due to geometric ambiguities inherent to the geometry of SAR images.

6 Conclusions

Using basic trigonometry and a few simple hypotheses, we implemented a method that successfully provides quantitative estimates of crater morphology changes. This new method overcomes some classic difficulties faced by optical instruments, which are hampered with clouds or daylight. It is also more robust and flexible than previous SAR methods, such as measurements derived from SAR shadows. The method is validated by comparing the measured depth with estimates from photogrammetry and SAR shadow methods for images from the 2002 eruption. All tools developed in the framework of this study are written in Python and freely available. They could be readily adaptable to other volcanoes hosting sub-circular crater(s).

This study confirms with quantitative measurements that the 2021 crater collapse of Nyiragongo is significantly deeper than it was after the 2002 eruption. However, due to the narrow shape of its bottom, its volume is only 15-20 % larger. The unprecedented density of the time series of SAR images acquired during the 2021 collapse also reveals that it occurred episodically over a few days while a dike was propagating. Comparing collapse timing with ash emissions also provides hints on the post-eruptive mechanisms.

Open Research Section

All data used in this study are available here `https://doi.org/10.5281/zenodo.7755707`. PickCraterSAR is available on Github : `https://github.com/mjaspard/pick_app.git`.

Acknowledgments

Sentinel-1 SAR images data are provided by ESA. ALOS-2 SAR images are provided by JAXA under the terms and conditions of the Second Earth Observation Research Announcement (PI No. ER2A2N086). We acknowledge S. Sobue and Y. Aoki for assisting in the quick response of JAXA. CSK images were obtained from ASI through the GEO GSNL Supersite initiative. We thank M. Poland, S. Ebmeier and M. Bonano for having helped unlock the delivery of CSK images to the Virunga Supersite, and C. Tinel and C. Proy (French Centre National d'Etude Spatiales (CNES)) for facilitating coordination between the scientific response and space agencies participating in the United Nation (UN) "Space and Major Disasters" International Charter. TerraSAR-X SAR images were obtained from DLR through the International Charter "Space and Major Disasters" (© DLR e.V. 2021, Distribution Airbus DS Geo GmbH). ICEYE images were obtained in the framework of the ECTIC project funded by BELSPO. Capella imagery is copyright of the Capella Space company, all rights reserved. Access to Capella imagery is subject to licence agreement, which can be requested from the Capella company. RCM data is provided by the Canadian Space Agency under the "Approved end-user" licence terms. ERS and ENVISAT archives were provided by ESA in the frame of Cat-1 projects no C1P.3224 RADARSAT-1 archives were obtained from Earth Observation Data Managment System (EODMS) from NRCAN. P. de Buyl, L. Clarisse and N. Clerbaux helped obtain SEVIRI data provided by EUMETSAT. R. Grandin acknowledges support from project FAIR-EASE, funded by the European Union's Horizon Europe Framework Programme (HORIZON-INFRA-2021-EOSC-01-04) under grant agreement No. 101058785. T. Shreve acknowledges support from a Carnegie Postdoctoral Fellowship (2021-2022). PickCraterSAR had been developed using PyQt5. This manuscript benefited from fruitful discussions with J. Barrière on the crater morphology.

References

Barrière, J., d'Oreye, N., Oth, A., Geirsson, H., Mashagiro, N., Johnson, J. B., ... Kervyn, F. (2018). Single-station seismo-acoustic monitoring of nyiragongo's lava lake activity (dr congo). *Frontiers in Earth Science*, 82.

Barrière, J., d'Oreye, N., Smets, B., Oth, A., Delhaye, L., Subira, J., ... others (2022). Intra-Crater Eruption Dynamics at Nyiragongo (DR Congo), 2002–2021. *Journal of Geophysical Research: Solid Earth*, *127*(4), e2021JB023858.

Clarisse, L., Coheur, P.-F., Prata, F., Hadji-Lazaro, J., Hurtmans, D., & Clerbaux, C. (2013). A unified approach to infrared aerosol remote sensing and type specification. *Atmospheric Chemistry and Physics*, *13*(4), 2195–2221.

Dualeh, E., Ebmeier, S., Wright, T., Albino, F., Naismith, A., Biggs, J., ... Roca, A. (2021). Analyzing explosive volcanic deposits from satellite-based radar backscatter, volcán de fuego, 2018. *Journal of Geophysical Research: Solid Earth*, *126*(9), e2021JB022250.

Dualeh, E., Ebmeier, S., Wright, T., Poland, M., Grandin, R., Stinton, A., & Camejo-Harry, M. (2021). Dome growth at la soufriere, st. vincent quantified from synthetic aperture radar backscatter. In *Agu fall meeting abstracts* (Vol. 2021, pp. V14A–08).

Durieux, J. (2002). The pre-2002 activity-volcano nyiragongo (dr congo): Evolution of the crater and lava lakes fron the discovery to the present. *The pre-2002 activity-Volcano Nyiragongo (DR Congo): Evolution of the Crater and Lava Lakes fron the Discovery to the Present*, 1000–1008.

Komorowski, J., Tedesco, D., Kasereka, M., Allard, P., Papale, P., Vaselli, O., ... others (2002). The January 2002 flank eruption of Nyiragongo volcano (Democratic Republic of Congo): Chronology, evidence for a tectonic rift trigger, and impact of lava flows on the city of Goma. *The January 2002 eruption-The January 2002 flank eruption of Nyiragongo Volcano (Democratic Republic of Congo): chronology, evidence for a tectonic rift trigger, and impact of lava*

flows on the city of Goma, 1000–1035.

Lev, E., Ruprecht, P., Oppenheimer, C., Peters, N., Patrick, M., Hernández, P. A., ... Marlow, J. (2019). A global synthesis of lava lake dynamics. *Journal of Volcanology and Geothermal Research*, *381*, 16–31.

Liégeois, M., & Luntumbue, M. (2022). *Défis et enjeux du plan de retrait de la MONUSCO.*

Massonnet, D., & Feigl, K. L. (1998). Radar interferometry and its application to changes in the earth's surface. *Reviews of geophysics*, *36*(4), 441–500.

Moore, C., Wright, T., Hooper, A., & Biggs, J. (2019). The 2017 eruption of erta'ale volcano, ethiopia: Insights into the shallow axial plumbing system of an incipient mid-ocean ridge. *Geochemistry, Geophysics, Geosystems*, *20*(12), 5727–5743.

Muñoz, V., Walter, T. R., Zorn, E. U., Shevchenko, A. V., González, P. J., Reale, D., & Sansosti, E. (2022). Satellite radar and camera time series reveal transition from aligned to distributed crater arrangement during the 2021 eruption of cumbre vieja, la palma (spain). *Remote Sensing*, *14*(23), 6168.

Pallister, J. S., Schneider, D. J., Griswold, J. P., Keeler, R. H., Burton, W. C., Noyles, C., ... Ratdomopurbo, A. (2013). Merapi 2010 eruption—chronology and extrusion rates monitored with satellite radar and used in eruption forecasting. *Journal of Volcanology and Geothermal Research*, *261*, 144–152.

Pottier, Y. (1978). Première éruption historique du Nyiragongo et manifestations adventives simultanées du Volcan Nyamulagira (Chaîne des Virunga-Kivu-Zaire: Décembre 76-Juin 77). [Rapport Annuel]. *Musée Royal de l'Afrique Centrale (Tervuren, Belgium)*, 157–175.

Rivalta, E., & Segall, P. (2008). Magma compressibility and the missing source for some dike intrusions. *Geophysical Research Letters*, *35*(4).

Smittarello, D., Smets, B., Barrière, J., Michellier, C., Oth, A., Shreve, T., ... others (2022). Precursor-free eruption triggered by edifice rupture at nyiragongo volcano. *Nature*, *609*(7925), 83–88.

Tazieff, H. (1977). An exceptional eruption: Mt. Nyiragongo, January 10th. *Bulletin of Volcanology*, *40*(3), 189-200.

Wadge, G., Saunders, S., & Itikarai, I. (2012). Pulsatory andesite lava flow at bagana volcano. *Geochemistry, Geophysics, Geosystems*, *13*(11).

Wauthier, C., Cayol, V., Kervyn, F., & d'Oreye, N. (2012). Magma sources involved in the 2002 nyiragongo eruption, as inferred from an insar analysis. *Journal of Geophysical Research: Solid Earth*, *117*(B5).

Figure01.

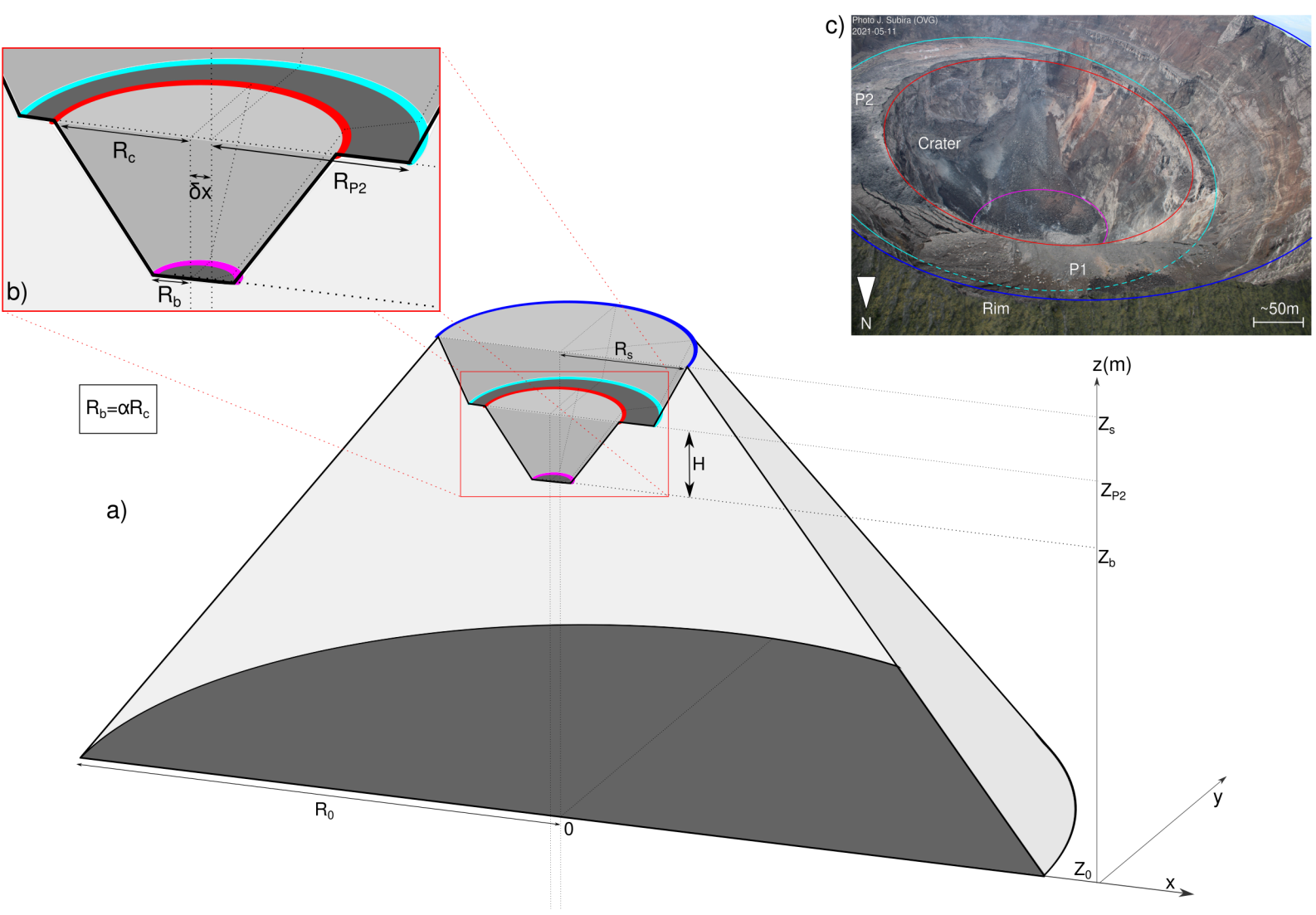
b)
R_c
δx
R_{P2}
R_b
c)
Photo J. Subira (OVG)
2021-05-11
P2
Crater
P1
Rim
N
~50m
a)
$R_b=\alpha R_c$
R_s
H
z(m)
Z_s
Z_{P2}
Z_b
R_0
0
Z_0
y
x

Figure02.

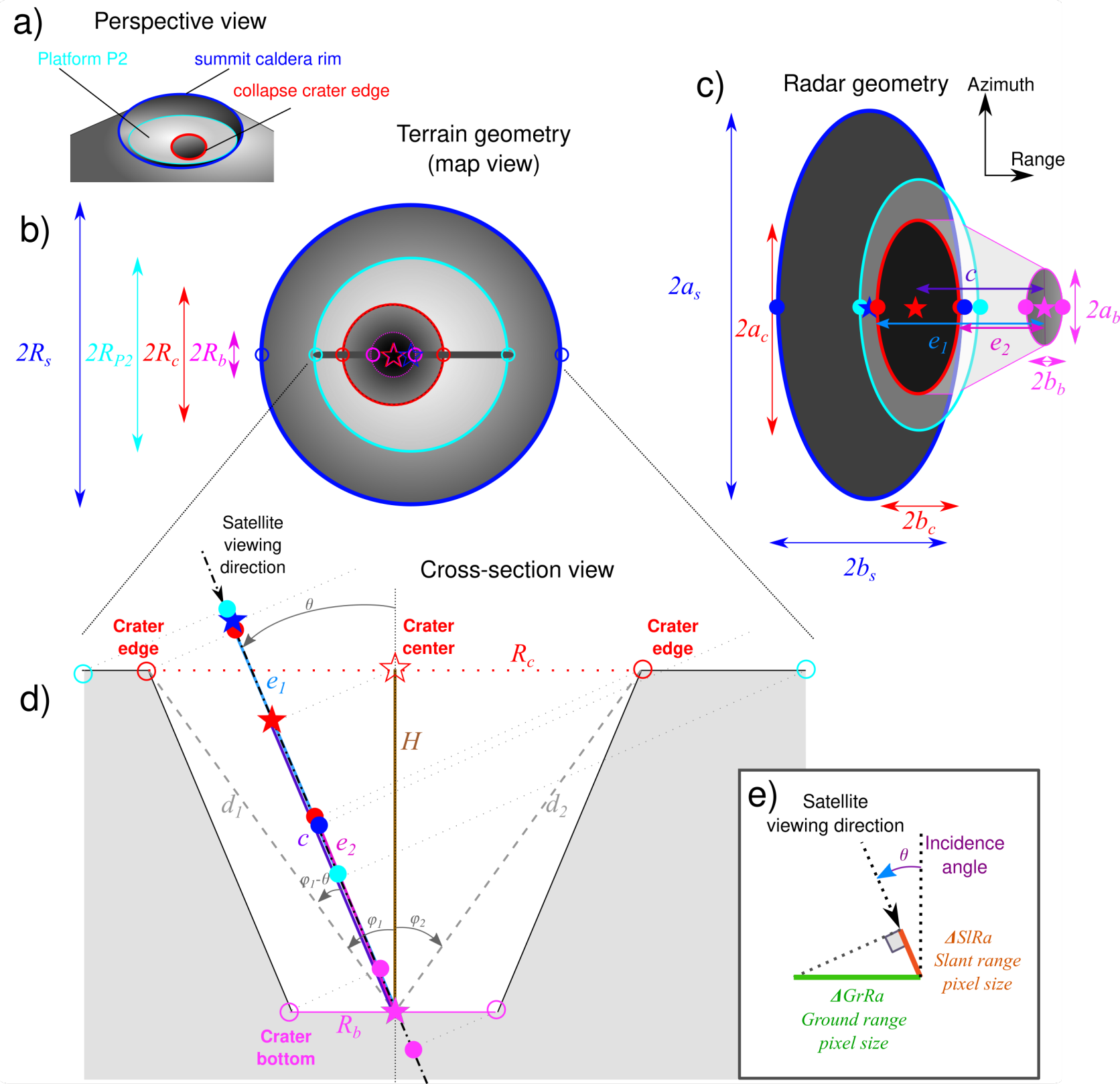
a)
Perspective view
Platform P2
summit caldera rim
collapse crater edge
Terrain geometry
(map view)
b)
$2R_s$
$2R_{P2}$
$2R_c$
$2R_b$
c)
Radar geometry
Azimuth
Range
$2a_s$
$2a_c$
c
e_1
e_2
$2a_b$
$2b_b$
$2b_c$
$2b_s$
Satellite
viewing
direction
Cross-section view
d)
Crater
edge
Crater
center
Crater
edge
θ
R_c
e_1
H
d_1
d_2
c
e_2
φ_1-θ
φ_1
φ_2
Crater
bottom
R_b
e)
Satellite
viewing direction
Incidence
angle
θ
ΔSlRa
Slant range
pixel size
ΔGrRa
Ground range
pixel size

Figure03.

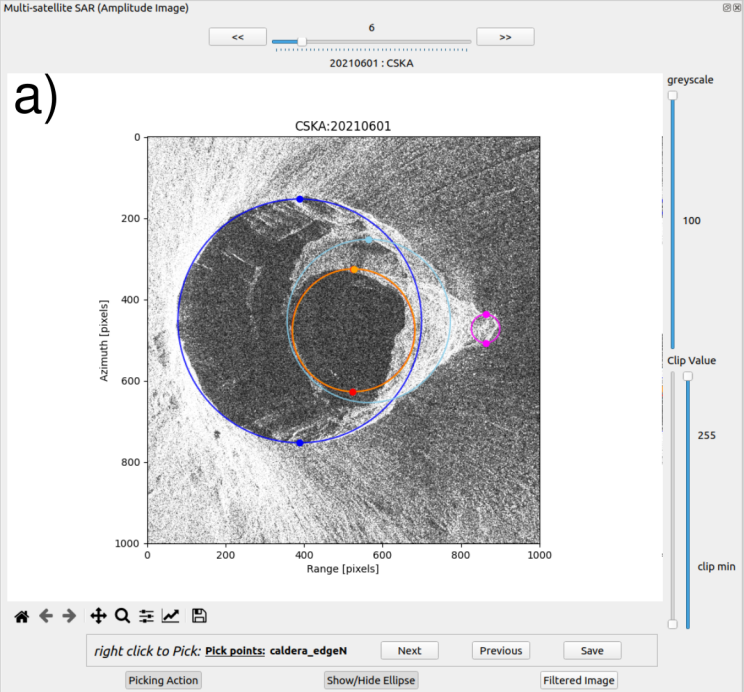
Multi-satellite SAR (Amplitude Image)
<<
6
>>
20210601 : CSKA
a)
CSKA:20210601
Azimuth [pixels]
Range [pixels]
greyscale
100
Clip Value
255
clip min
right click to Pick: Pick points: caldera_edgeN
Next
Previous
Save
Picking Action
Show/Hide Ellipse
Filtered Image

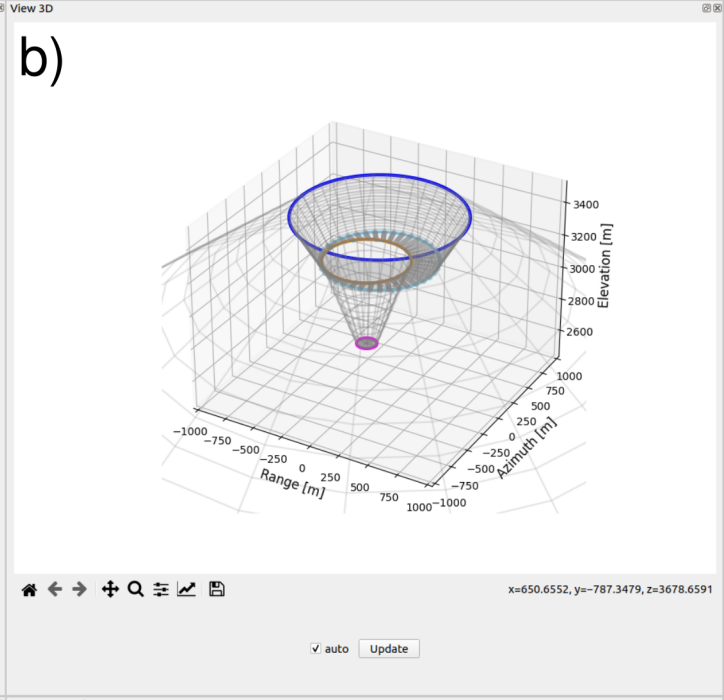
View 3D
b)
Elevation [m]
Range [m]
Azimuth [m]
x=650.6552, y=−787.3479, z=3678.6591
auto
Update

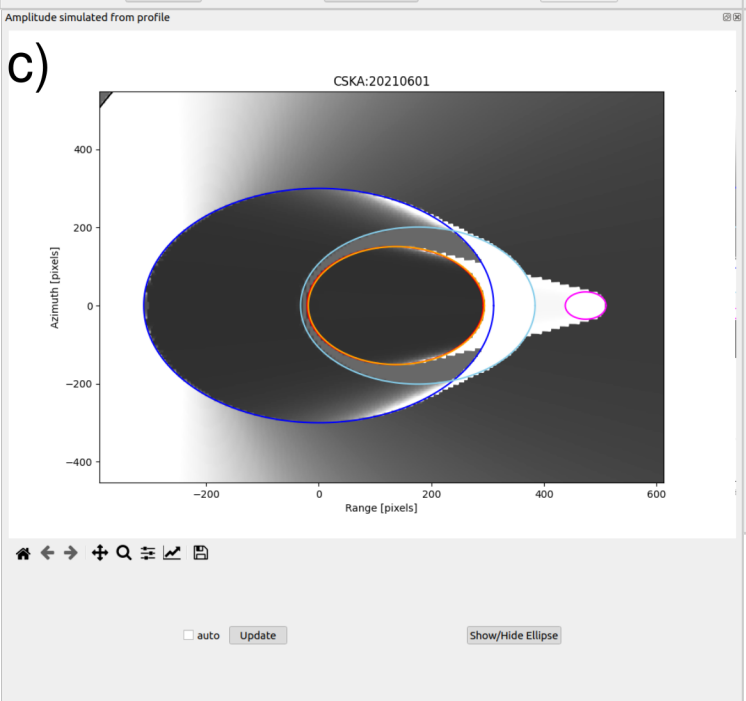
Amplitude simulated from profile
c)
CSKA:20210601
Azimuth [pixels]
Range [pixels]
auto
Update
Show/Hide Ellipse

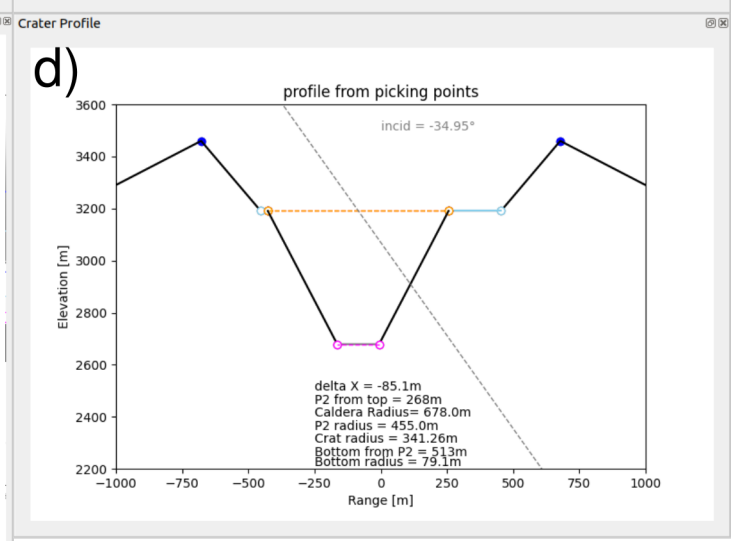
Crater Profile
d)
profile from picking points
incid = -34.95°
Elevation [m]
Range [m]
delta X = -85.1m
P2 from top = 268m
Caldera Radius= 678.0m
P2 radius = 455.0m
Crat radius = 341.26m
Bottom from P2 = 513m
Bottom radius = 79.1m

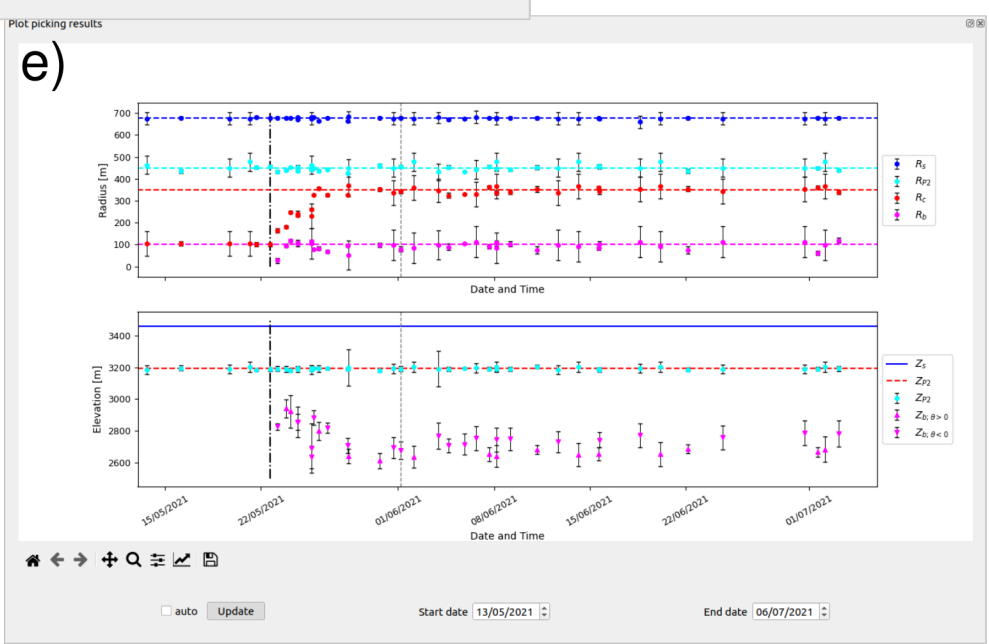
Plot picking results
e)
Radius [m]
Date and Time
Elevation [m]
15/05/2021
22/05/2021
01/06/2021
08/06/2021
15/06/2021
22/06/2021
01/07/2021
auto
Update
Start date 13/05/2021
End date 06/07/2021

Figure04.

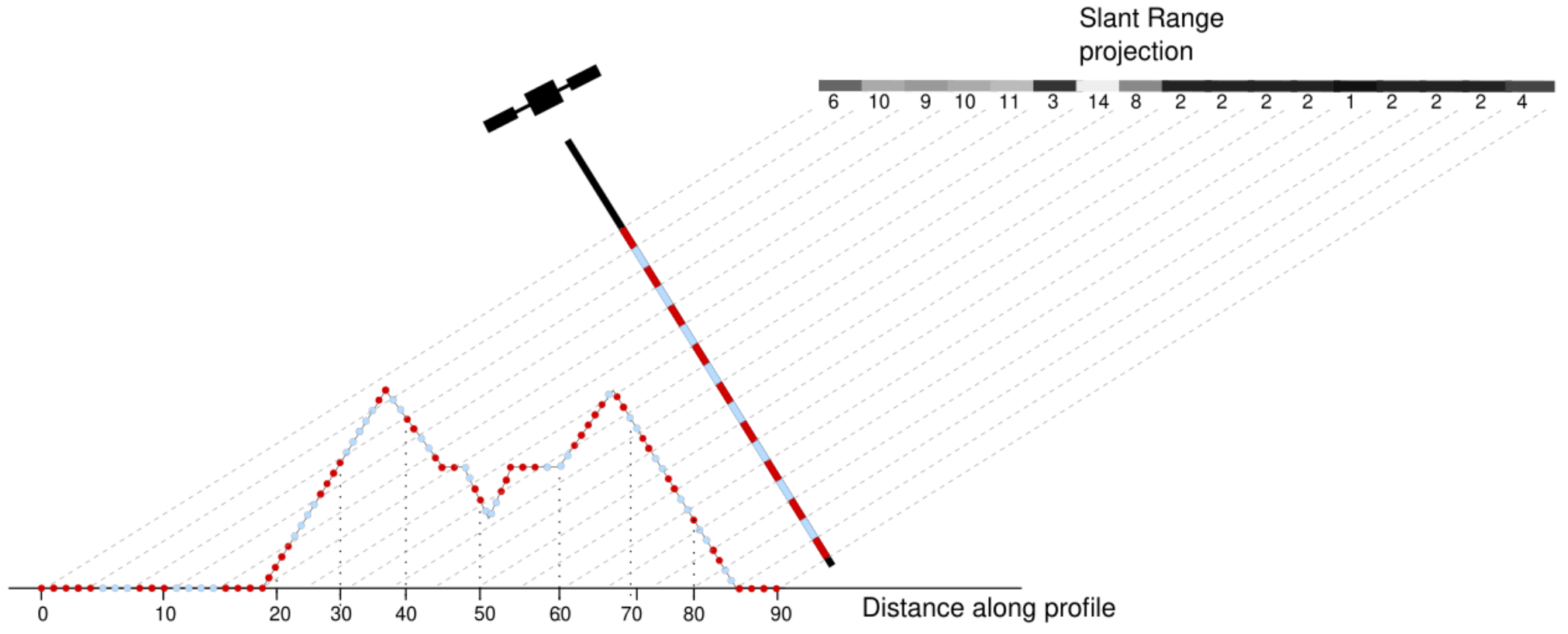
Slant Range
projection
6 10 9 10 11 3 14 8 2 2 2 2 1 2 2 2 4
0 10 20 30 40 50 60 70 80 90
Distance along profile

Figure05.

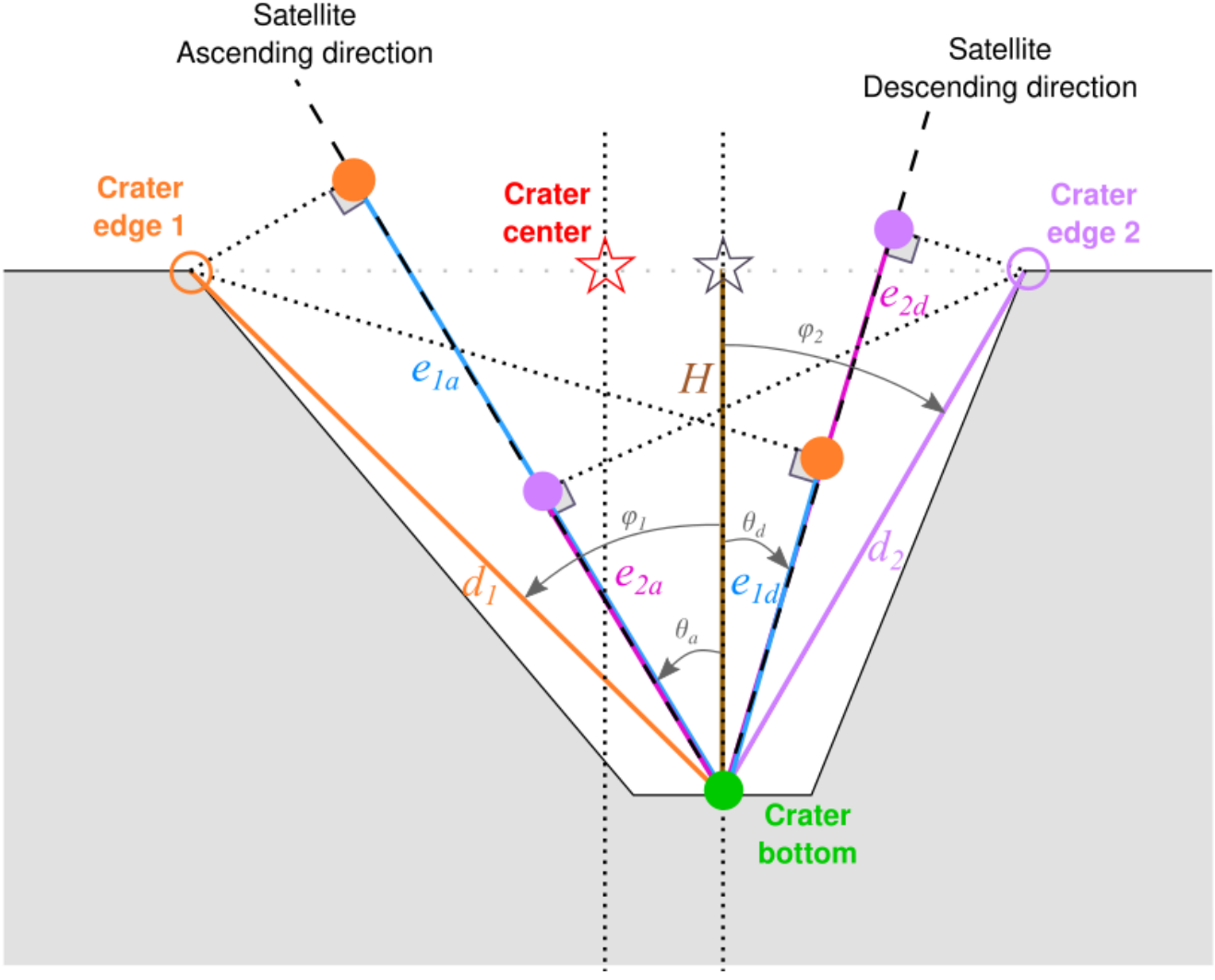
Satellite
Ascending direction
Satellite
Descending direction
Crater
edge 1
Crater
center
Crater
edge 2
e_{1a}
e_{2d}
φ_2
H
φ_1
θ_d
d_1
e_{2a}
e_{1d}
d_2
θ_a
Crater
bottom

Figure06.

a)

Eruption

Ash Peaks

(1) (2) (3)

Radius (m)

R_s R_c R_{P2} R_b

Ash index

2021-05-15 2021-05-22 2021-06-01 2021-06-08 2021-06-15 2021-06-22 2021-07-01 2021-07-08

b)

Elevation (m)

Z_s Z_{P2} Z_b^{2002} Z_{P2} $Z_{b;\theta>0}$ $Z_{b;\theta<0}$ Z_b^{assym}

Depth (m)

2021-05-15 2021-05-22 2021-06-01 2021-06-08 2021-06-15 2021-06-22 2021-07-01 2021-07-08

c)

Volume ($10^6 m^3$)

$V^{\alpha}_{trunc};\theta>0$ $V^{\alpha}_{trunc};\theta<0$ V_{cone} V_{cyl}

2021-05-15 2021-05-22 2021-06-01 2021-06-08 2021-06-15 2021-06-22 2021-07-01 2021-07-08